

# Dynamics of PC3 Cancer Cells in Self-Generated Hypoxia

*Kimberly Shen*

Junior Paper  
Department of Physics  
Princeton University  
Fall 2022



Advisor: Professor Robert H. Austin  
Second Reader: Professor Peter D. Meyers

This paper represents my work in accordance with University regulations.

/s/ Kimberly Shen

## **Abstract**

A novel phosphorescence-based oxygen sensor in combination with cell segmentation and tracking software was used to examine the motility of PC3 cancer cells under self-generated hypoxia. Measurements of the speed of PC3 cell motion were positively correlated with local oxygen concentrations, gradient magnitudes and consumption rates. Furthermore, PC3 cells with very large size demonstrated slightly increased motility throughout hypoxic regions in comparison to small PC3 cells. Lastly, the directions of the PC3 cell movements did not show any obvious correlations with oxygen concentration gradient directions, suggesting that the PC3 cells did not perform aerotaxis in spite of the lethally hypoxic conditions generated by the cells.

# Contents

<b>1</b>	<b>Introduction</b>	<b>1</b>
<b>2</b>	<b>Preliminaries</b>	<b>1</b>
2.1	Self-induced hypoxia procedure . . . . .	1
2.2	Data issues . . . . .	2
2.2.1	Uneven illumination . . . . .	2
2.2.2	Other issues . . . . .	3
2.3	Summary of usable data . . . . .	5
<b>3</b>	<b>Oxygen concentration analysis</b>	<b>6</b>
3.1	Oxygen concentration sensor . . . . .	6
3.1.1	Fluorescence and phosphorescence . . . . .	6
3.1.2	Phosphorescence quenching . . . . .	7
3.2	Sensor calibration . . . . .	9
3.2.1	Calibration measurements . . . . .	10
3.2.2	Pixel value to $[O_2]$ conversion . . . . .	11
3.3	Oxygen gradients . . . . .	12
3.4	Oxygen consumption rate . . . . .	13
<b>4</b>	<b>Cell motility analysis</b>	<b>14</b>
4.1	Cell segmentation validation . . . . .	16
4.2	Cell sizes . . . . .	17
4.3	Directionality of cell movement . . . . .	17
<b>5</b>	<b>Results</b>	<b>19</b>
5.1	SH Trial Results . . . . .	19
5.2	LH Trial Results . . . . .	21
5.2.1	Oxygen concentration vs. gradient magnitude . . . . .	24
<b>6</b>	<b>Conclusion</b>	<b>25</b>
	<b>References/Acknowledgements</b>	<b>28</b>

## 1 Introduction

Around 90% of all cancer deaths are caused by metastasis, the spreading of cancer cells from the primary tumor site to distant locations in the body [1]. Therefore a comprehensive understanding of the cellular mechanisms governing metastasis is of crucial interest in developing effective cancer treatments and improving clinical outcomes. Unfortunately metastasis is an enormously complex process that remains poorly understood despite decades of research. Based on our current knowledge, two processes that have been implicated in metastasis so far are the epithelial-mesenchymal transition (EMT) [2] and the generation of polyclonal cancer cells (PACCs) [3].

The EMT is a process where cancerous epithelial cells begin showing properties characteristic of mesenchymal cells. More specifically the cancer cells lose their cell-to-cell adhesions and become more motile, enhancing their ability to invade surrounding tissues [2]. PACCs are cancer cells that have doubled (or  $n$ -pled,  $n \geq 2$ ) their genomic content. PACCs are typically very large in size and are hypothesized to increase the evolvability of a given cancer cell population due to their enhanced ability to generate heritable variation [4]. Increased evolvability in turn allows the cancer cell population to resist medical treatment and adapt to new environmental conditions following migration away from a primary tumor site, facilitating metastasis.

Viewing EMT and PACC formation (and, more generally, the development of metastatic potential) as a response of cancer cells to stress it is natural to investigate the dynamics of cancer cells under the environmental stressors typically present in a tumor. One well-documented feature of tumors is intratumoral hypoxia [5]. Intratumoral hypoxia results from the failure of blood vasculature to sufficiently permeate a rapidly growing tumor and the relatively small diffusion limit of oxygen within tissues (around 150  $\mu\text{m}$ ) [6]. It follows that the cancer cells within any moderately-sized tumor are immersed in a remarkably hypoxic environment.

In this paper we will investigate the effects of hypoxia on cancer cell motility (as a potential indicator of EMT) and on cell size (as a potential indicator of PACC formation). In particular, we will subject cancer cells to self-generated hypoxia, that is, hypoxic conditions resulting from the cancer cells' own metabolism, closely resembling the process that occurs naturally in tumors. Previous studies have attempted to create hypoxic conditions by either purging the cell environment of oxygen or by using cobalt chloride ( $\text{CoCl}_2$ ). However, the former method suffers from an inability to create oxygen gradients which have a crucial presence in tumors and the latter method is merely mimetic: it induces a hypoxia-like response in cells by stabilizing certain protein factors but does not physically decrease ambient oxygen levels [7]. Lastly, both methods are externally imposed rather than emergent from the tumor itself, giving uncertainty to the applicability of the observed cell responses to the behavior of cells in real tumors.

## 2 Preliminaries

### 2.1 Self-induced hypoxia procedure

PC3 cells are an epithelial cell line obtained from an advanced prostate cancer metastasis [8]. We used PC3 cells expressing green fluorescent protein (GFP) in the cytosol, allowing convenient fluorescence microscopy imaging of the cells. The cells were cultured to surface confluence in a culture flask at 37°C, then passaged using trypsin and then transferred to a 35 mm Lumox gas-permeable culture dish. The dish was then mounted on a 30 mm diameter glass cover slip spin-coated with a phosphorescence-based oxygen concentration sensor (see §3.1 for more details). The sandwich setup ensured that the sensor was responsive to cell culture O<sub>2</sub> levels from above

rather than the ambient oxygen from below (see Figure 1(a)).

The sandwich setup was then mounted onto a microscope stage. Starting at this point and continuing until the end of the experiment, an image of the plate was taken every hour. Due to the large size of the plate relative to the field of view of the microscope, a  $6 \times 6$  stitching of the microscope images was required to obtain an image of the entire plate. The images were also taken in two modes: a green fluorescent protein (GFP) filter was used to image the PC3 cells and an mCherry (mCh) filter was used to image the phosphorescence intensity of the oxygen sensor. An Andor Zyla VSC-02965 camera with a 500 ms exposure time was used to capture the images.

The cells were incubated on the microscope stage for 24 hours allowing the cells to attach to the bottom of the culture dish and form a confluent layer. During this pre-hypoxia period the culture dish was fully exposed to ambient atmospheric oxygen concentration and a GFP image was taken every hour. Then a round acrylic plug with the dimensions shown in Figure 1(b) was placed over the confluent layer, cutting off the environmental oxygen supply for cells in the center of the plate and allowing them to become hypoxic. During this hypoxia period an image was taken every hour in both GFP and mCh modes. Around 24 hours later the acrylic plug was removed allowing the plate to once again be exposed to ambient atmospheric oxygen concentration, alleviating the hypoxic conditions. During the post-hypoxia period, images in GFP mode were taken every hour.

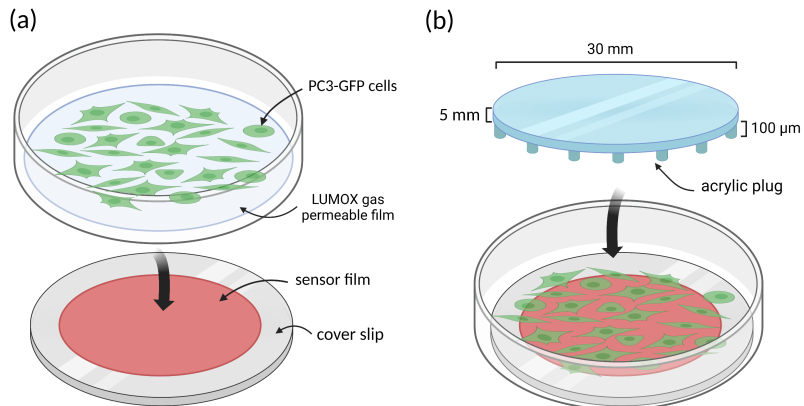


Figure 1: Experimental setup.

## 2.2 Data issues

A number of issues with data collection and analysis were encountered during the experiment. In this section we address each issue and the steps taken to resolve them as best as possible. Note that throughout this paper we will use the standard axes directions as used in image processing.

### 2.2.1 Uneven illumination

Both the GFP and mCh images suffered from uneven illumination across the field of view of the microscope. Resultantly, each sub-image tended to be more dimly lit along its edges than

its center. Stitching the sub-images together then created an artificial grid-like structure on the images (see Figure 2).

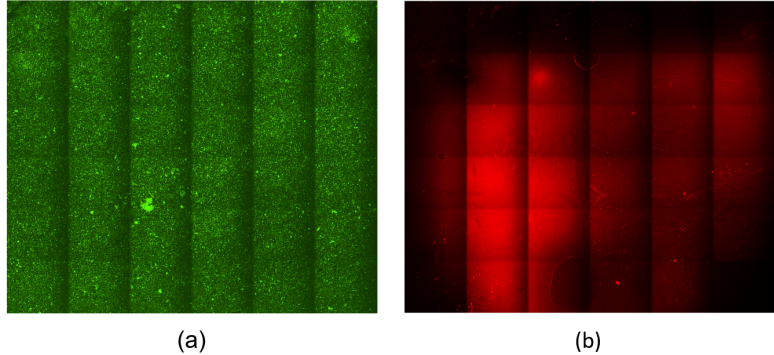


Figure 2: Example image showing uneven illumination on the (a) GFP and (b) mCh images.

This issue was particularly problematic for the mCh images since their pixel values were intended to accurately measure local oxygen concentrations. We dealt with this issue by using a sampling approach to generate an estimate of the mCh image had it been taken at a uniform illumination intensity. Under the assumption that the uneven illumination distribution was consistent across all sub-images and across time, then pixel values  $p(x_0, y_0)$  sampled from a fixed coordinate  $(x_0, y_0)$  within each sub-image could be assumed to have been taken at the same illumination intensity. We then performed a 2D curve fit to the sampled spatial location and pixel value data which was used to generate a new image for the phosphorescence intensity. This new image was then used for all subsequent analysis instead of the initial mCh image.

Due to high levels of noise in the mCh images we chose to measure the median pixel value over a region rather than individual pixel values. In more detail, for each sub-image, the median pixel value from a  $1000 \times 1000$  pixel square centered at  $(700, 700)$  within each sub-image was used to estimate the pixel value at  $(700, 700)$ . More succinctly,

$$p(700, 700) \approx \text{median}\{p(700 + i, 700 + j) \mid i, j \in [-500, 500]\} \quad (1)$$

The coordinates of the sampling squares were chosen to coincide with the most brightly-lit region of each sub-image, where the illumination intensity is relatively uniform. We then used the Curve Fitter app in MATLAB to fit a two-variable polynomial of degree 5 to the 36 sampled points and then generated a new image from the fitted polynomial. The workflow is illustrated in Figure 3.

For the GFP images, the wide illumination range resulted in difficulty with accurately tracking cells located in regions of highly differing illumination intensity. To optimize accuracy and consistency of cell tracking we limited the scope of our tracking to the most brightly and uniformly illuminated regions of the image i.e.  $1000 \times 1000$  pixel squares centered at  $(700, 700)$  within each sub-image (see Figure 4). Note that due to high cell density and the large size of the GFP images, we were still able to track a large number of cells (5000 to 10000) within each GFP image despite the limited tracking area.

### 2.2.2 Other issues

A few other issues were also encountered:

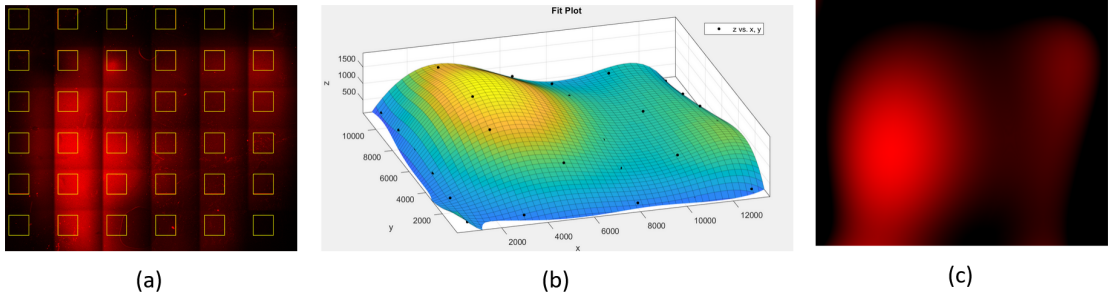


Figure 3: (a) Original mCh image with overlay of the square sampling regions (b) Curve fit generated by MATLAB (c) Corrected mCh image

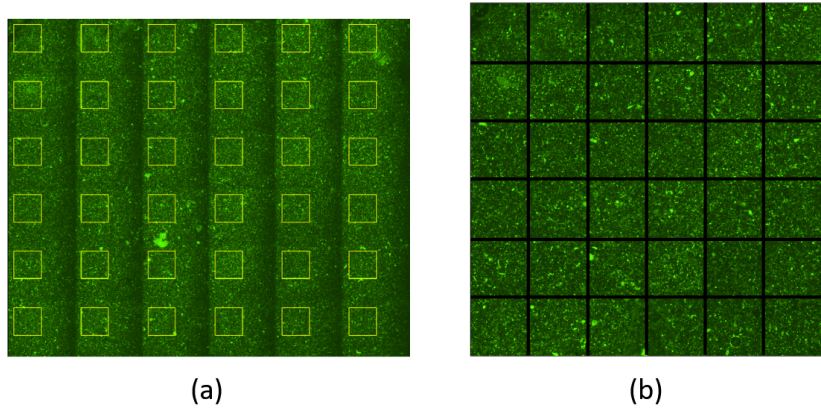


Figure 4: (a) A GFP image with an overlay consisting of squares enclosing the regions in which cell tracking was performed. (b) New GFP image consisting of the only selected squares. The squares have been separated by grid lines of exaggerated thickness for illustration purposes. Note the relatively uniform illumination intensity across all the squares.

*mCh image saturation:* For the oxygen sensor used in our experiment, lower oxygen concentration results in stronger phosphorescence intensity (see §3.1). Unfortunately, in one of the trials the phosphorescence intensity was sufficiently high to saturate some pixel values in the mCh images in highly hypoxic regions. We resolved this issue by removing saturated pixel values from the collection of sampling points used to approximate the uniformly illuminated mCh image in the previous section. The polynomial fit for the remaining data points was then used to approximate the pixel values in the saturated regions.

*Image stitching:* Nikon Elements-based software was used to stitch together the 36 sub-images based on alignment of overlapping regions. However for the GFP images, even very slight differences (on the order of a few pixels) in the stitching of spatially adjacent sub-images over time is problematic because it can artificially introduce cell movement. We resolved this issue by using the Linear Stack Alignment with SIFT plugin in ImageJ on default settings to independently register the GFP sampling square within each sub-image over time before conducting cell tracking [9].

*Apoptosis:* Apoptosis (programmed cell death) occurred in the PC3 cells after several hours of

hypoxia, as indicated visually by blebbing (see Figure 5(b)) Cell tracking could not be meaningfully continued after apoptosis onset due to possible mistaking of blebbing as cell movement. We thus had to limit our cell tracking to early stages of hypoxia exposure. We were also unable to resume cell tracking in the post-hypoxia period due to difficulty with distinguishing cells from blebs.

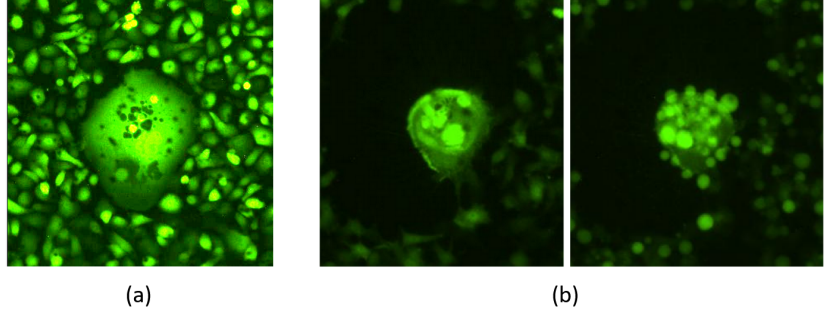


Figure 5: (a) A gigantic PC3 cell (possibly a PACC) surrounded by average-sized PC3 cells (b) Apoptosis with blebbing of the same gigantic PC3 cell after several hours under self-generated hypoxia. Average-sized PC3 cells also demonstrated blebbing but somewhat less prominently than gigantic cells.

### 2.3 Summary of usable data

To conclude this section on preliminaries we provide an summary of the two experimental trials whose data were used for our analysis. One trial involved a relatively long hypoxic period (33 hours) and the other a relatively short one (18 hours) which we will henceforth denote LH and SH, respectively. For each trial the precise durations of the pre-, mid- and post-hypoxia periods is given in the table below as well as initial cell density and the time of apoptosis onset.

Trial	SH	LH
Pre-hypoxia (hours)	16	15
Mid-hypoxia (hours)	18	33
Post-hypoxia (hours)	58	88
Apoptosis onset (hours)	6	16
Initial cell density (cells mm <sup>-2</sup> )	894.83	514.15

Table 1: The SH and LH trials were performed by Professor Robert H. Austin at Princeton University and took place on May 16–20, 2021 and May 23–28, 2021 respectively. The time of apoptosis onset is measured relative to hypoxia onset.

Initial cell density was measured by performing a cell segmentation on the first mid-hypoxia GFP image (see section §4.1). Note that the conversion of 1 pixel side length = 1.0833  $\mu\text{m}$  was used to convert the density to physical units. The LH trial likely had a later apoptosis onset as well as slower hypoxia development than the SH trial due to the lower initial cell density and thus lower oxygen metabolism.

We ultimately only performed cell tracking on images taken during the first 6 hours of hypoxia in the SH trial due to apoptosis onset. For the LH trial, we only performed cell tracking on the

first 8 hours of hypoxia due to difficulty with approximating the mCh images accurately over an increasingly large region of saturated pixel values.

### 3 Oxygen concentration analysis

We begin the analysis by examining the local oxygen concentrations present in the Lumox culture dish as a function of space and time. In this section, we will demonstrate that a phosphorescence-based oxygen sensor provides a simple method of measuring oxygen concentrations with high spatiotemporal resolution. We will then show how  $[O_2]$  gradients and the  $O_2$  consumption rate of the PC3 cells can be estimated.

#### 3.1 Oxygen concentration sensor

In 2018 Zhao *et al* developed a novel  $O_2$  sensor which was used in our experiment. The sensor was synthesized by dissolving the platinum-based  $O_2$  sensor dye Pt(II) *meso*-tetrakis(pentafluorophenyl) porphine (PtTFPP) in poly(perfluoroether) (PFPE) [10]. For brevity we will henceforth refer to this sensor as the PtTFPP/PFPE sensor. In this section we will provide an overview of the basic physical chemistry underlying the mechanism of the oxygen sensor.

##### 3.1.1 Fluorescence and phosphorescence

To begin, a singlet state of a molecule is defined as a molecule where all of the molecule's electrons are paired. More specifically, if the molecule contains an electron with quantum numbers  $(n, l, m, m_s)$  then it also contains an electron with quantum numbers  $(n, l, m, -m_s)$ . As a result, the molecule has net spin  $S = 0$  and no spin degeneracy [11]. In contrast, a triplet molecule contains a single pair of unpaired electrons. As a result, the molecule has net spin  $S = 1$  giving rise to a  $2S + 1 = 3$ -fold spin degeneracy [11].

Fluorescence and phosphorescence are based on transitions between different excited states of a molecule. To visualize such transitions it is convenient to use a Jablonski diagram, some examples of which are given in Figure 6. Distinct energy levels are depicted by horizontal lines. The thick horizontal lines denote the singlet ground state ( $S_0$ ) and the singlet ( $S_1$ ) and triplet ( $T_1$ ) excited states of the molecule with their relative energy levels. The thinner horizontal lines denote vibrational excited modes within each energy level. Solid arrows denote radiative excitation/decay processes i.e. processes that involve absorption or emission of a photon. Squiggly arrows denote non-radiative excitation/decay processes.

First observe that the ground state is a singlet state, which is true for most atoms and molecules [12]. One notable exception is molecular oxygen  $O_2$  which has a triplet ground state at room temperature [13]. Also notice that the  $T_1$  state has lower energy than the  $S_1$  state. In general, "the origin of the energy difference lies in the effect of spin correlation on the Coulombic interactions between electrons" [12]. Figure 6 is thus generally applicable to many fluorophores (molecules that fluoresce) and phosphors (molecules that phosphoresce).

The mechanism of fluorescence is as follows: a fluorophore is excited via absorption of a photon, typically to an excited vibrational state:  $S_0 + h\nu_a \rightarrow S_1$ . Vibrational relaxation to the lowest energy vibrational mode occurs rapidly ( $\sim 10^{-12}$  sec) in comparison to the fluorescent lifetime of the molecule i.e. the time spent in the  $S_1$  state ( $\sim 10^{-8}$  sec). The fluorophore then decays back to the ground state (typically to an excited vibrational mode before decaying to the lowest energy mode) and emits a photon:  $S_1 \rightarrow S_0 + h\nu_e$  [13]. From the Jablonski diagram it is clear

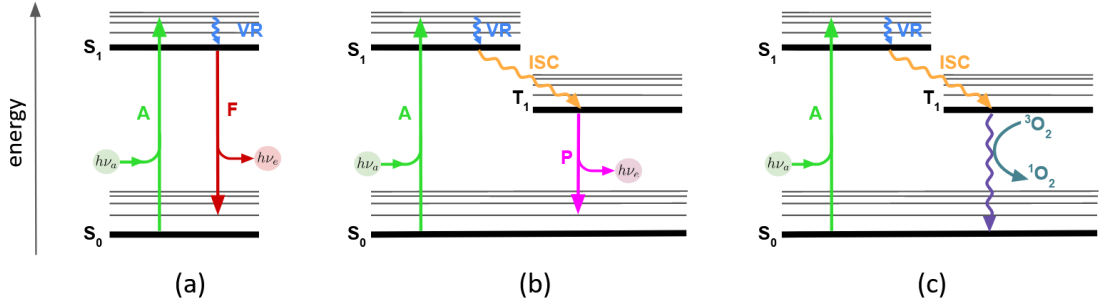


Figure 6: Jablonski diagram for a typical molecule undergoing (a) fluorescence, (b) phosphorescence or (c) phosphorescence quenching by  ${}^3\text{O}_2$ . The abbreviations are A for absorbance, VR for vibrational relaxation, F for fluorescence, ISC for inter-system crossing, and P for phosphorescence. Note that  $h\nu_a$  denotes absorbed photons and  $h\nu_e$  denotes emitted photons.

that  $\nu_e > \nu_a$ . Hence the light emitted via fluorescence typically has a longer wavelength than the excitation wavelength, a phenomenon known as the Stokes shift.

The mechanism of phosphorescence is similar: a phosphor absorbs a photon, reaching an excited state and relaxes to the lowest energy vibrational mode:  $S_0 + h\nu_a \rightarrow S_1$ . The phosphor then undergoes an intersystem crossing defined as the transition  $S_1 \rightarrow T_1$ . Since the  $T_1$  state has spin  $S = 1$  while the  $S_0$  has spin  $S = 0$ , the transition  $T_1 \rightarrow S_0 + h\nu_e$  is forbidden by conservation of spin and thus occurs on a much longer time scale. As a result, the phosphorescence lifetime of the phosphor (the time spent in the  $T_1$  state) is remarkably long ( $\sim 10^{-3}$  sec for PtTFPP) in comparison to typical fluorescence lifetimes ( $\sim 10^{-8}$  sec).

Many substances can undergo either fluorescence and phosphorescence upon excitation. Thus, a relevant quantity to consider is quantum yield defined as the probability that atom or molecule will undergo a desired photochemical reaction [13]. For example, the fluorescence quantum yield is the probability that an absorbed photon will later result in the emission of a photon via fluorescence.

Some desirable properties of PtTFPP (which were verified using photon counting equipment at Shenzhen University by Professor Robert H. Austin) are that it demonstrates strong singlet absorbance in the green spectral range and has close to 100% intersystem crossing from the singlet excited state to the triplet excited state. As a result, upon activation by green light PtTFPP has an essentially 0% fluorescence quantum yield and 100% phosphorescence quantum yield in the red spectral range in the absence of other decay processes. Thus, the Nikon mCherry filter set is well-suited for measuring the phosphorescence intensity of PtTFPP (see Figure 7) and the emitted light can be assumed to be free of fluorescence artefacts.

### 3.1.2 Phosphorescence quenching

Phosphorescence quenching is defined as any process that decreases phosphorescence intensity [13]. The essential mechanism of the PtTFPP/PFPE oxygen sensor is collisional phosphorescence quenching by oxygen. Although the precise mechanism currently is not well understood, triplet ground state oxygen is a powerful phosphorescence quencher [13]. The following non-radiative reaction occurs following a collision between a PtTFPP dye molecule (D) and a dissolved oxygen

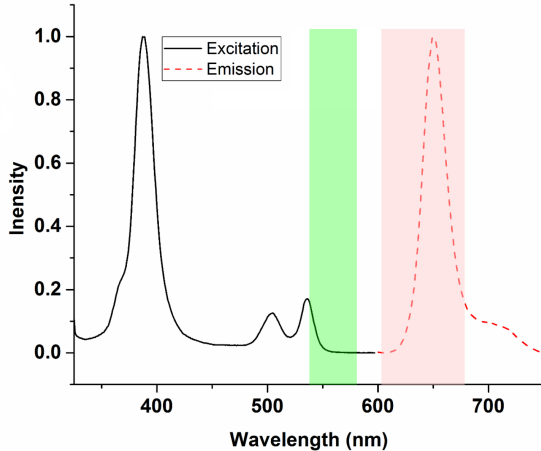
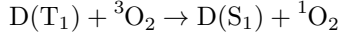


Figure 7: Excitation and emission spectra of 10  $\mu\text{g}/\text{ml}$  PtTFPP in dichloromethane (a compound used to synthesize the PFPE matrix). The Nikon mCherry filter set has excitation wavelength range 542 to 582 nm and emission wavelength range 603 to 678 nm which are indicated by the shaded regions.

molecule:



where  ${}^3\text{O}_2$  denotes triplet ground state oxygen and  ${}^1\text{O}_2$  denotes singlet ground state oxygen (see Figure 6(c)). The excited singlet oxygen then deactivates rapidly in aqueous solution ( $\sim 3\text{ }\mu\text{s}$ ), regenerating triplet oxygen [14]. In summary, oxygen molecules can prevent the PtTFPP dye from emitting photons via phosphorescence. Hence, in the mCh images dimmer regions indicate regions of high oxygen concentration while brighter regions indicate regions of low oxygen concentration.

In general the concentration of a collisional quenching agent ( $\text{O}_2$  in this case) and the phosphorescence intensity of the phosphor are related by the Stern-Volmer equation [13]:

$$\frac{I_0}{I} = 1 + k_q \tau_0 [\text{O}_2]$$

where  $I$  is the phosphorescence intensity,  $I_0$  is the phosphorescence intensity at anoxia ( $[\text{O}_2] = 0$ ),  $\tau_0$  is the phosphorescence lifetime of the phosphor at anoxia and  $k_q$  is the rate constant governing the quenching reaction. The constant  $k_q$  is largely controlled by oxygen diffusion rates [14]. Thus to optimize the sensitivity of the sensor for trace oxygen concentration sensing we must maximize the Stern-Volmer constant  $K_{\text{SV}} = k_q \tau_0$ . Since  $k_q$  and  $\tau_0$  are essentially independent then this is equivalent to maximizing  $k_q$  and  $\tau_0$  separately.

From this condition it is clear that the PtTFPP/PFPE sensor is well-suited to measuring trace oxygen concentrations. The triplet state of PtTFPP has an relatively long intrinsic lifetime ( $\tau_0 > 1\text{ ms}$ ) compared to other phosphorescent dyes and PFPE is characterized by high gas permeability (increasing quenching efficiency). The PtTFPP/PFPE sensor is also well suited to long-term *in vitro* study of cell culture oxygen levels due to the high photostability of PtTFPP and low biological toxicity of PFPE. Thus, we will now turn to the task of calibrating the sensor.

### 3.2 Sensor calibration

In principle, the Stern-Volmer equation could be used to determine  $[O_2]$  as a function of  $I$  if the values of  $I_0$  and  $K_{SV} = k_q\tau_0$  were known. We will follow a slightly more general approach that is essentially identical to the Stern-Volmer model but relaxes the assumption that the fraction of excited phosphors is small at any concentration of the quencher. In the process of doing so, we will also give a derivation of the Stern-Volmer equation.

Define the following variables:

- $[D]$  is the concentration of all PtTFPP molecules (singlet and triplet)
- $[T_1]$  is the concentration of triplet PtTFPP molecules
- $\varphi$  is the oxygen concentration normalized such that  $\varphi = 1$  indicates normoxia defined as equilibrium  $[O_2]$  for an aqueous solution exposed to atmospheric oxygen concentrations ( $P_{O_2} = 0.21$  atm) at  $37^\circ C$ .
- $k_0$  is the intrinsic decay rate of triplet PtTFPP molecules via phosphorescence
- $k_q$  is the rate at which  $O_2$  molecules quench triplet PtTFPP molecules
- $k_p$  is the excitation rate of singlet PtTFPP molecules

Given the near 100% phosphorescence quantum yield of PtTFPP in the absense of quenching, then the population of PtTFPP molecules in singlet or triplet states can be fully controlled by three processes: excitation, phosphorescence and quenching. It follows that

$$\frac{d[T_1]}{dt} = -k_0[T_1] - k_q\varphi[T_1] + k_p([D] - [T_1]).$$

At a given  $\varphi$  we may assume that  $[T_1]$  reaches a quasi-steady state i.e.  $\frac{d[T_1]}{dt} = 0$ . Now let  $I$  be the emitted phosphorescence intensity. Since  $I = k_0[T_1]$  then we may eliminate  $[T_1]$  from the above expression and solve for  $I$  which gives

$$I = \frac{k_p[D]}{1 + \frac{k_q}{k_0}\varphi + \frac{k_p}{k_0}}.$$

We therefore expect  $I(\varphi)$  to be a function of the form

$$I(\varphi) = \frac{a}{\varphi + b} \tag{2}$$

where  $a$  and  $b = (1 + \frac{k_p}{k_0})\frac{k_0}{k_q} = \frac{k_0 + k_p}{k_q}$  are positive numbers whose values can be determined by fitting a curve to calibration measurements. Setting  $\varphi = 0$  gives  $I_0 = \frac{a}{b}$  so

$$\begin{aligned} \frac{I_0}{I} &= \frac{a}{b} \cdot \frac{\varphi + b}{a} \\ &= 1 + \frac{\varphi}{b}. \end{aligned}$$

It follows that the sensitivity of the sensor can be quantified by  $b^{-1} = \frac{k_q}{k_0 + k_p}$ . Since  $k_p$  is fixed then  $b^{-1}$  is maximized when  $k_q$  is maximized and  $k_0 = \tau_0^{-1}$  is minimized.<sup>1</sup> Thus the conditions

---

<sup>1</sup>We claim that  $\tau_0 = k_0^{-1}$ . To see this note in the absence of any quenchers and excitation sources that

for maximizing trace oxygen sensitivity are equivalent in this model and in the model governed by the Stern-Volmer equation.

To derive the Stern-Volmer equation we must make the additional assumption that only a small fraction of PtTFPP molecules are excited to the triplet state. Then we can approximate  $[D] - [T_1] \approx [D]$  so

$$\frac{d[T_1]}{dt} = -k_0[T_1] - k_q\varphi[T_1] + k_p[D]$$

and using  $I = k_0[T_1]$  and  $\frac{d[T_1]}{dt} = 0$  gives

$$I = \frac{k_p[D]}{1 + \frac{k_q}{k_0}\varphi}.$$

Setting  $\varphi = 0$  shows that  $I_0 = k_p[D]$  and using  $\tau_0 = k_0^{-1}$  then gives

$$I = \frac{I_0}{1 + k_q\tau_0\varphi}. \quad (3)$$

and rearranging then gives the Stern-Volmer equation. Notice  $I(\varphi)$  must be of the form given in Equation 2 regardless of whether or not we assume that the fraction of excited triplet PtTFPP is small. We thus assume Equation 2 and proceed with calibration measurements to estimate the constants.

### 3.2.1 Calibration measurements

Calibration measurements were performed by exposing the PtTFPP/PFPE sensor to known concentrations of oxygen using a gas mixer of  $O_2$  and Ar and taking images of the sensor phosphorescence intensity through an mCherry filter. The calibration data was collected by Professor Robert H. Austin. We note that the images themselves give direct measurements of “camera counts” rather than phosphorescence intensity. However at fixed exposure time (500 m sec) and following subtraction of any background counts (36 counts, obtained from taking a blank image) we can assume that camera counts is proportional to phosphorescence intensity. Letting  $M$  indicate camera counts (with background counts already subtracted) we can then write

$$M(\varphi) = \frac{\alpha}{\varphi + \beta}$$

for some  $\alpha, \beta > 0$  (more specifically  $\alpha = a \frac{M(\varphi)}{I(\varphi)}$  and  $\beta = b$ ) to be determined by curve fitting. The results of the calibration measurements and the curve fit generated by MATLAB’s curve fitting toolbox are given in the log-log plot in Figure 8.

The curve fit gives values  $\alpha = 3.026$  with 95% confidence interval (2.645, 3.406) and  $\beta = 0.001321$  with 95% confidence interval (0.001117, 0.001526). The fit had a R-square value of 0.9927. To complete the calibration we will now derive an expression relating the pixel values of a given mCherry phosphorescence intensity image to the local oxygen concentrations.

---

$\frac{d[T_1]}{dt} = -k_0[T_1]$ . It follows that  $[T_1]_t = [T_1]_{t=0}e^{-k_0 t}$  so  $\tau_0 = k_0^{-1}$ .

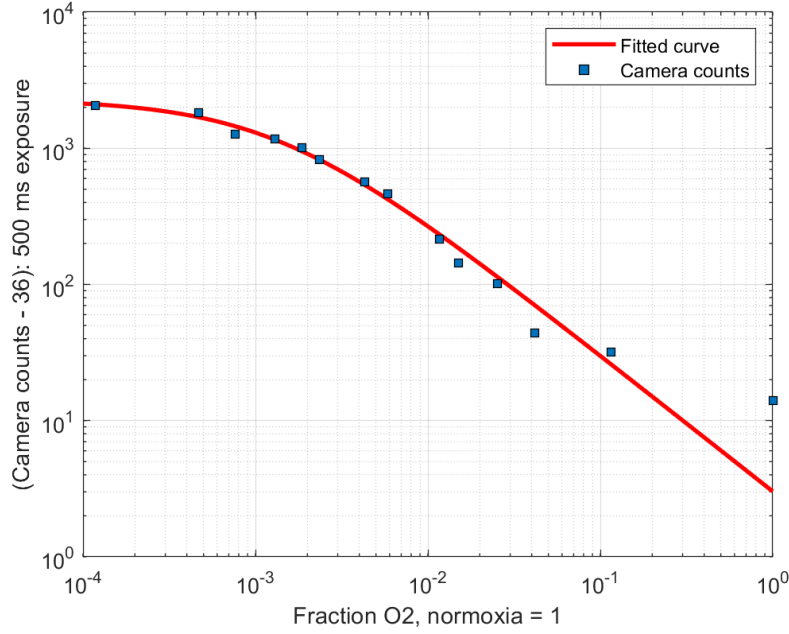


Figure 8: Calibration measurements. Note the fitted function for  $M(\varphi)$  assumes the form of a negative softplus function on the log-log plot as expected for a function of the form  $M(\varphi) = \frac{\alpha}{\varphi + \beta}$ .

### 3.2.2 Pixel value to [O<sub>2</sub>] conversion

Let  $p$  indicate the pixel values of the mCherry phosphorescence intensity image to be analyzed after subtraction of the background pixel value (107, obtained by taking a blank image). Due to differences in exposure times and variations in thickness of the PtTFPP/PFPE sensor between Lumox plates, it is not true in general that  $p(\varphi) = M(\varphi)$ . However we may use ratios to derive an expression for  $p(\varphi)$  from which we can obtain  $\varphi(p)$ , the desired conversion. Since we are interested in finding  $\varphi(p)$  let us consider  $M$  as a function of  $p$ :

$$M(p) = \frac{\alpha}{\beta + \varphi(p)}. \quad (4)$$

Now let  $p_0$  be the pixel value in a normoxic region of the mCh image. We may find  $p_0$  by measuring the median pixel value of the (corrected) mCh image taken immediately after the cell culture is plugged and before hypoxia development begins. Following this procedure we measured  $p_0 = 157.128$  for SH and  $p_0 = 391.831$  for LH.

Since all background values have been subtracted, then both  $M(p)$  and  $p$  are proportional to the phosphorescence intensity of the PtTFPP/PFPE oxygen sensor. It follows that  $p \propto M(p)$  as well and since  $M(p) \propto (\beta + \varphi(p))^{-1}$  by Equation 4 then

$$\frac{p}{p_0} = \frac{\beta + \varphi(p_0)}{\beta + \varphi(p)}.$$

Since  $\varphi(p_0) = 1$  by definition then solving for  $\varphi(p)$  gives

$$\varphi(p) = \frac{p_0(\beta + 1)}{p} - \beta. \quad (5)$$

Then using  $\beta = 0.001321$  and the measured values of  $p_0$  for each trial gives the desired conversions:

$$\begin{aligned}\varphi_{\text{SH}}(p) &= \frac{157.3356}{p} - 0.001321 \\ \varphi_{\text{LH}}(p) &= \frac{392.3486}{p} - 0.001321.\end{aligned}$$

Some examples of a (corrected) mCh image from each of the SH and LH trials after the conversions to oxygen concentrations is given in Figure 9.

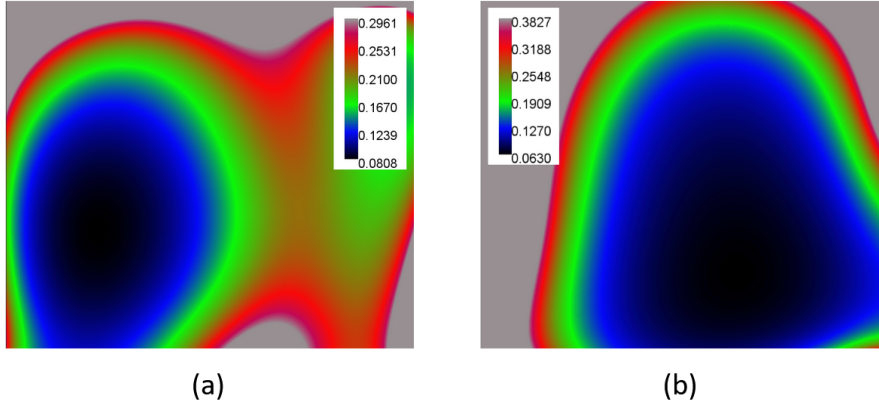


Figure 9: Spatial oxygen concentrations as measured by the PtTFPP/PFPE oxygen sensor in (a) the SH trial 3 hours after plugging and in (b) the LH trial 8 hours after plugging. The calibration bars show the oxygen concentrations normalized such that normoxia is normalized to 1.

### 3.3 Oxygen gradients

Using Equation 5 we can obtain the spatiotemporal oxygen concentrations of the cell culture from the mCherry phosphorescence intensity images. Let  $\varphi(x, y, t)$  be the concentration of  $O_2$  present in the experiment as a function of spatial position  $(x, y)$  and time  $t$ . Here  $x$  and  $y$  are measured in  $\mu m$  and  $t$  is measured in hours. Let  $d$  be the side length of a square image pixel in  $\mu m$ .

Although  $\varphi(x, y, t)$  is not a smooth function due to the discrete pixelization of images and the 1 hour time intervals between images, we can still approximate its first order partial derivatives by averaging the function's slopes between  $(x, y, t)$  and the relevant adjacent pixels. For example:

$$\frac{\partial \varphi}{\partial x} \approx \frac{1}{2} \left( \frac{\varphi(x+d, y) - \varphi(x, y)}{d} + \frac{\varphi(x, y) - \varphi(x-d, y)}{d} \right)$$

which simplifies to

$$\frac{\partial \varphi(x, y)}{\partial x} \approx \frac{\varphi(x + d, y) - \varphi(x - d, y)}{2d}.$$

The formulas for  $\frac{\partial \varphi(x, y)}{\partial y}$  and  $\frac{\partial \varphi(x, y)}{\partial t}$  are analogous. The magnitude of the gradient can then be calculated as

$$|\nabla \varphi(x, y)| = \sqrt{\frac{\partial \varphi(x, y)}{\partial x}^2 + \frac{\partial \varphi(x, y)}{\partial y}^2}.$$

Furthermore, we can approximate the second (non-mixed) partial derivatives using a Taylor series expansion:

$$\varphi(x + d, y) = \varphi(x, y) + \frac{\partial \varphi(x, y)}{\partial x} \cdot d + \frac{1}{2} \frac{\partial^2 \varphi(x, y)}{\partial x^2} \cdot d^2 + O(d^3).$$

It follows that

$$\frac{\partial^2 \varphi(x, y)}{\partial x^2} \approx \frac{\varphi(x + d, y) + \varphi(x - d, y) - 2\varphi(x, y)}{d^2}$$

and the formulas for  $\frac{\partial^2 \varphi(x, y)}{\partial y^2}$  and  $\frac{\partial^2 \varphi(x, y)}{\partial t^2}$  are analogous. With these formulas it also becomes straightforward to approximately the Laplacian  $\nabla^2 \varphi = \frac{\partial^2 \varphi}{\partial x^2} + \frac{\partial^2 \varphi}{\partial y^2}$  of the oxygen distribution which will be useful for estimating the oxygen consumption rate of the PC3 cells as we will show next.

### 3.4 Oxygen consumption rate

Let  $\tilde{\varphi}(x, y, t)$  be the concentration of  $O_2$  that is generated or consumed by the oxygen sources and sinks in the experiment. We will use the sign convention that  $\tilde{\varphi} > 0$  indicates that oxygen has been generated and  $\tilde{\varphi} < 0$  indicates that oxygen has been consumed. In this experiment, oxygen is generated by the inwards flow of  $O_2$  from the edges of the plug and is consumed by the metabolism of the PC3 cells. Under the conditions of mass conservation Fick's second law of diffusion states

$$\frac{\partial \varphi}{\partial t} - D \nabla^2 \varphi = 0$$

where  $D$  is the diffusion constant of oxygen in an aqueous solution at  $37^\circ C$  ( $2644 \mu m^2 s^{-1}$ ) [15]. Accounting for the oxygen sources and sinks in our experiment requires the addition of an extra term:

$$\frac{\partial \varphi}{\partial t} - D \nabla^2 \varphi = \frac{\partial \tilde{\varphi}}{\partial t}.$$

In the interior of the Lumox plate we may assume that there are no oxygen sources. Thus  $\frac{\partial \tilde{\varphi}}{\partial t}$  is the density of the rate of change in oxygen density solely due to the metabolism of the PC3 cells. Now let  $\Omega$  be any 2D spatial region contained in the interior of the lumox plate. We can take a surface integral to calculate the change in the amount of oxygen contained in  $\Omega$  resulting

from PC3 cell metabolism:

$$\begin{aligned}\frac{d}{dt} \oint_{\Omega} \tilde{\varphi} dA &= \oint_{\Omega} \frac{\partial \tilde{\varphi}}{\partial t} dA \\ &= \oint_{\Omega} \left( \frac{\partial \varphi}{\partial t} - D \nabla^2 \varphi \right) dA.\end{aligned}$$

Alternatively, we may apply Stokes' theorem to the previous result to obtain

$$\frac{d}{dt} \oint_{\Omega} \tilde{\varphi} dA = \oint_{\Omega} \frac{\partial \varphi}{\partial t} dA - D \oint_{\partial\Omega} \nabla \varphi \cdot d\mathbf{n}.$$

This method requires calculation of a line integral of  $\nabla \varphi \cdot d\mathbf{n}$  instead of a surface integral of  $\nabla^2 \varphi$ . However, given the greater ease of computing surface integrals for images we will primarily use the former equation. In particular, we can calculate the oxygen consumption rate of a given cell occupying an area  $\Omega_{\text{cell}}$  as

$$\frac{d}{dt} \oint_{\Omega_{\text{cell}}} \tilde{\varphi} dA = \oint_{\Omega_{\text{cell}}} \left( \frac{\partial \varphi}{\partial t} - D \nabla^2 \varphi \right) dA.$$

This concludes our overview of the oxygen concentration distribution analysis from the mCherry phosphorescence intensity images. We continue with an overview of our analysis of the GFP-filter images of the PC3 cells.

## 4 Cell motility analysis

We next turn to the task of investigating the size and motility of the PC3 cells. Given the enormous number of cells present in each image ( $10^4$  to  $10^5$ ) this task clearly could not be done by hand and was instead performed using two computer-based programs: Cellpose and TrackMate.

Cellpose is a deep learning-based cell segmentation algorithm [16].<sup>2</sup> Since our PC3 cells were fluorescently labeled by cytoplasmic proteins we chose to use the “cyto” (short for cytoplasm) model and otherwise used default settings to segment our raw GFP images of PC3 cells. We then generated label images from the cell segmentation (see Figure 10).<sup>3</sup>

After obtaining label images, we used the ImageJ plugin TrackMate [17] to track the motion of the cells over time. In particular we obtained the displacements of the cells between temporally adjacent label images. TrackMate’s displacements are measured as the euclidean distance between the centers of the linked cells at distinct time points [18]. An example of the TrackMate-facilitated process of linking cells in label images is shown in Figure 11.

In Figure 11(a), the cells (outlined in magenta) in the two label images generated from GFP images taken one hour apart are shown. Some of the cells have moved slightly between the

---

<sup>2</sup>Cell segmentation refers to the process of splitting an image up into regions, each of which is the area occupied by a individual cell.

<sup>3</sup>A label image is an image where all pixels contained in a cell region are given a uniform value. Additionally, to distinguish distinct cells, each cell in the image is given a unique pixel value. Unfortunately, the label images we worked with were unable to account for regions were multiple cells overlap.

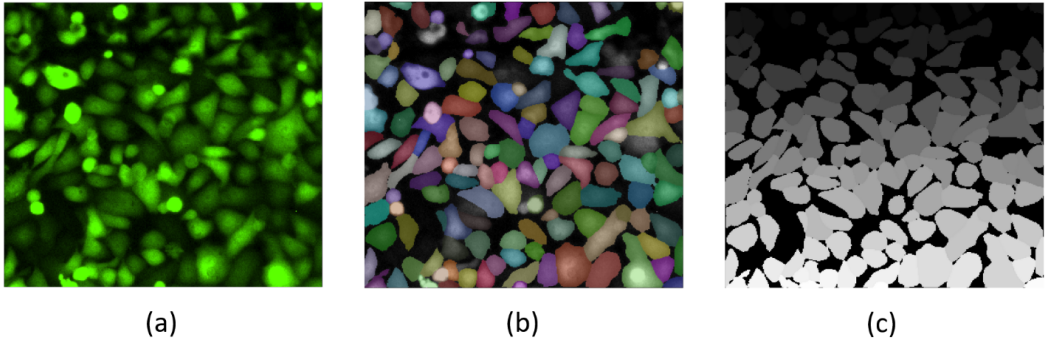


Figure 10: Cellpose-facilitated process of generating label images from raw cell. Shown above are (a) a sample raw GFP image, (b) Cellpose segmentation of the GFP image via the cyto model and (c) a label image generated from the cell segmentation.

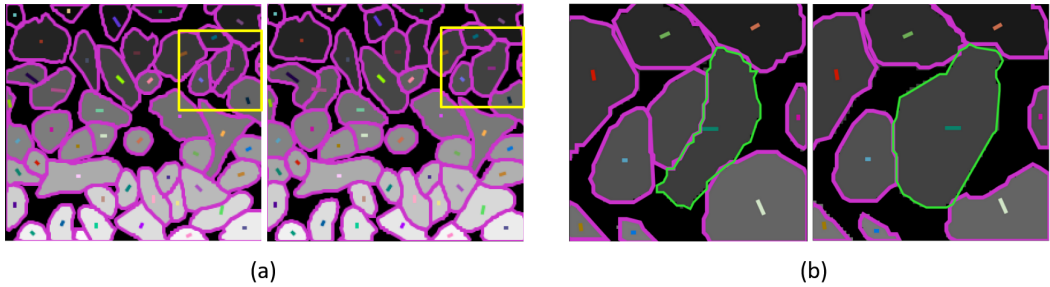


Figure 11: TrackMate-linked label images are shown in (a). The yellow boxed regions of the images contain a slightly large cell which was segmented incorrectly. The regions are blown up in (b). Two cells linked by TrackMate are highlighted in green. The apparent “displacement” between the two cells (illustrated by the dark green line) is erroneous.

two images. The rainbow lines connect the centers of cells linked between the images as corresponding to the motion of a single cell. TrackMate thus offers a simple method to measure cell displacements between images. However, TrackMate’s measurements are susceptible to errors when linking cells, particularly following segmentation errors.

For example, in Figure 11(b), a segmentation error resulted in an erroneous track. Notice that the large cell in the center of the image on the right had been erroneously segmented into two distinct cells in the image on the left. TrackMate then linked the cells highlighted in green in each image and recorded the “displacement” between the linked cells (illustrated by the dark green line segment). Clearly, the perceived displacement is primarily due to the segmentation error rather than true movement of the cell.

To improve accuracy for tracking the cell displacements (particularly for large cells) we implemented an “area check” on the cell displacement data. In particular, we fixed an area-limiting ratio  $r = 1.5$ . Then if the areas of a tracked cell at two different time points are given by  $A_1$  and  $A_2$ , we discarded the displacement data unless both inequalities  $\frac{A_1}{r} < A_2 < A_1r$  were satisfied. We also evaluated an additional performance metric to quantify the performance of the cellpose segmentation algorithm in general on our data as discussed next.

## 4.1 Cell segmentation validation

Although cellpose is one of the most high-performing cell segmentation algorithms currently available for free use [16], we performed additional validation testing of the cell segmentation algorithm on our PC3 cell data to ensure that our results reflect a “true” signal rather than some artefacts of the segmentation process.

We performed the identical benchmark testing procedure as was used in the original cellpose paper by Stringer *et al.* The segmentation of the PC3 cells by cellpose was compared to a ground truth segmentation performed by hand. Following Stringer *et al* we calculated the average precision (AP) at varying matching thresholds as  $AP = \frac{TP}{TP+FP+FN}$  where TP, FP, and FN indicates the number of true positives, false positives and false negatives, respectively, that occurred while segmenting several hundred sample cells [16].

The values of TP, FP and FN were counted as follows: a false negative was counted if cellpose failed to make any attempt to segment the cell. If cellpose gave a cell segmentation then a matching threshold was used to determine whether the segmentation corresponded to a true positive or a false positive. The matching threshold was the standard intersection over union (IoU) as used in computer imaging. For two regions  $R_1$  and  $R_2$  of an image, their intersection over union is defined as  $\text{IoU}(R_1, R_2) = \frac{\text{Area}(R_1 \cap R_2)}{\text{Area}(R_1 \cup R_2)}$ . If  $R_1$  is the ground truth segmentation of a cell and  $R_2$  is the cellpose segmentation of a cell then the segmentation was classified as a true positive if  $\text{IoU}(R_1, R_2) > t$  where  $t$  is some given threshold, and otherwise the segmentation was classified as false positive.

Stringer *et al* used a plot of  $AP(t)$  vs  $t$  for various values of  $t \in [0.5, 1]$  to compare the segmentation performance of cellpose with other segmentation programs [16]. We will compare the cellpose segmentation of our PC3 cells with Stringer *et al*’s data. To obtain a sample of cells to segment we used a list of 100 randomly-generated spatiotemporal coordinates and found the nearest cell to each coordinate. Since the vast majority of the PC3 cells are roughly similar in size and the cells also cover most of the image surface then we can assume that the sample is representative of the segmentation of the entire image.

For each sampled cell we calculated the IoU of the cellpose segmentation with the ground truth segmentation of the same cell. The procedure was repeated for both the SH and LH trials. The results are given in Figure 12, overlaid on the results of the original cellpose paper [16]. In general, cellpose performed well with segmenting our data, particularly for the LH trial. For moderate IoU threshold values, cellpose performed comparably well on our LH images as a specialist model on specialized data. For the SH trial, cellpose’s performance was comparable to a generalist model on generalized data. The superior performance of cellpose on the LH trial was likely due to its more in-focus images in comparison to the SH trial.

We note that cellpose performed relatively poorly in both trials at high IoU thresholds, indicating that cellpose often fails to match cell boundaries with the ground truth to high precision. This can be explained by the nature of the fluorescent PC3 cell images. In the GFP images, the PC3 cells do not have distinct edges (e.g. a clearly defined outer membrane) defining their boundaries but rather a relatively steep gradient in pixel values. As a result, there is some ambiguity when defining the exact boundaries of the cell in the ground truth segmentation. Thus, extremely precise matches between the cellpose segmentation and the ground truth become highly unlikely.

Nonetheless, the solid performance of cellpose at lower IoU thresholds confirms its ability to estimate cell boundaries and hence areas to reasonable precision, perhaps limited more by cell boundary ambiguity rather than algorithm faults. In fact, our primary motivation for obtaining

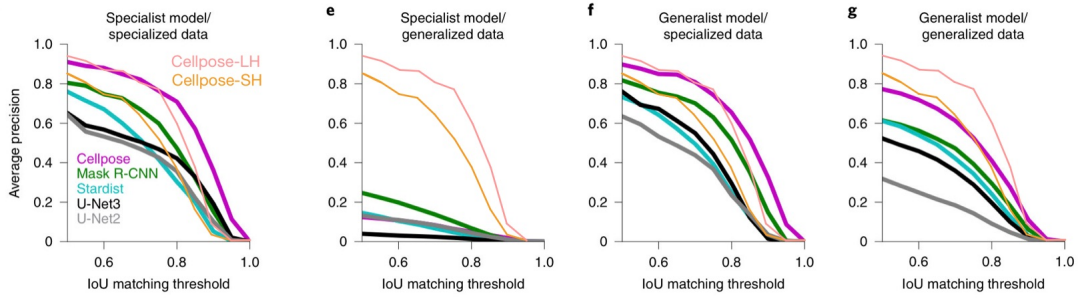


Figure 12: Segmentation performance of cellpose on our GFP images of PC3 cells in comparison to the performance of cellpose and other segmentation algorithms as reported in the original cellpose paper. In the figure, a generalist model refers to a cellpose algorithm trained to segment a wide variety of cell types while a specialist model refers to an cellpose algorithm trained to segment a specific cell type.

a cell segmentation of the GFP images was to obtain data on the sizes of the PC3 cells.

## 4.2 Cell sizes

A simple analysis that can be performed following cell segmentation is an examination of the distribution of the sizes of the PC3 cells. We use the area occupied by each cell in an image as a proxy for its true three-dimensional size. There are shortcomings to this proxy as the cells sometimes overlap or are cut off at the edges of the image, reducing their perceived area. However, the fraction of such cells is small (around  $10^{-1}$  to  $10^{-2}$  based on the sample of cells used in the image segmentation validation). A logarithmic histogram of cell sizes of the SH and LH trials at various times is given below in Figure 13.

The SH trial had more noticeable decrease in counts across all cell sizes during the hypoxia period from  $t = 2$  to  $t = 5$  with the total number of tracked cells falling from 9432 to 6742. In comparison, during the LH trial the total number of tracked cells was 8374 at  $t = 2$  and 7936 at  $t = 7$ . This may be due to the more extreme and rapidly-developed hypoxia during the SH trial causing more rapid cell death or possibly the better quality of cell segmentation (lower false negative rate) for the LH trial at later times.

## 4.3 Directionality of cell movement

A question of particular interest for us was whether the direction of PC3 cell movement showed any correlation with the direction of the local oxygen gradients in the vicinity of the cell. Given the severe hypoxia generated in the central region of the Lumox plate, it would be reasonable to hypothesize that the cells would attempt to move towards higher oxygen concentrations by following local  $[O_2]$  gradients.

For any given cell we can obtain its displacement in the  $x$  and  $y$  directions between times  $t$  and  $t + 1$  from the TrackMate data. We also can obtain the oxygen gradients at the cell's location from the oxygen sensor images. Thus we define the following:

- $\hat{r} = (r_x, r_y)$  is the displacement vector of a cell normalized to unit length
- $\hat{\varphi} = (\varphi_x, \varphi_y)$  is the average  $[O_2]$  gradient over the area occupied by the cell normalized to

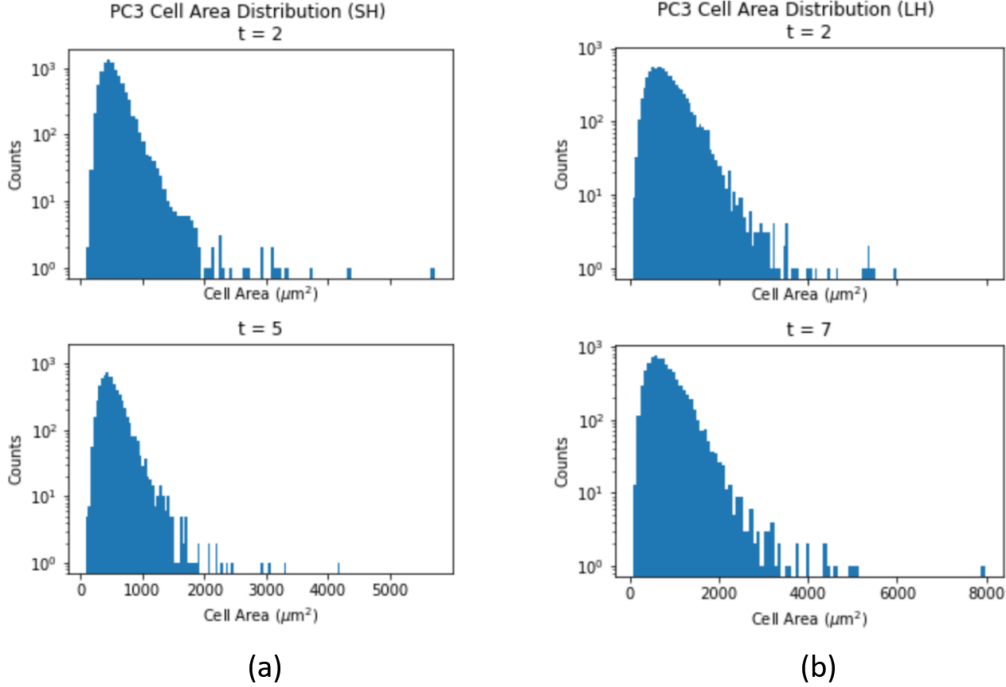


Figure 13: Cell size distribution of the PC3 cells at two hours after the onset of hypoxia and after 5 and 7 of hypoxia exposure in the (a) SH and (b) LH trials, respectively.

unit length

- $\theta$  is the angle of  $\hat{r}$  with respect to  $\hat{\varphi}$  with the sign convention that angles opening clockwise are positive

The sign convention for the angles was chosen to be consistent with the standard directions of the  $x$ - and  $y$ -axes as used in image processing (see Figure 14).

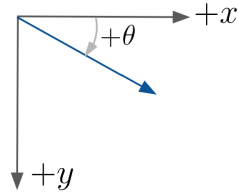


Figure 14: Standard axes directions used in image processing.

Lastly, to ensure that  $\theta$  is well-defined we restrict  $\theta$  to the (almost) symmetrical range  $[\pi, -\pi]$  where  $\theta = 0$  if and only if  $\hat{\varphi} = \hat{r}$ . We find the magnitude of  $\theta$  as follows:

$$|\theta| = \cos^{-1}(\hat{\varphi} \cdot \hat{r}) = \cos^{-1}(\varphi_x r_x - \varphi_y r_y)$$

where the cosine function is inverted over the interval  $[0, \pi]$ . For all angles  $\theta \neq \pi$ , we can find the sign of  $\theta$  by viewing  $\hat{\varphi}$  and  $\hat{r}$  as the three dimensional vectors  $(\varphi_x, \varphi_y, 0)$  and  $(r_x, r_y, 0)$ ,

respectively, and using a cross product and the sign function:<sup>4</sup>

$$\operatorname{sgn} \theta = \operatorname{sgn} (\hat{\varphi} \times \hat{r})_z = \operatorname{sgn} (\varphi_x r_y - \varphi_y r_x).$$

For the edge case  $\theta = |\theta| = \pi$  we have  $\operatorname{sgn} \theta = 1$  even though  $(\hat{\varphi} \times \hat{r})_z = 0$  so this case must be treated separately. In summary,

$$\operatorname{sgn} \theta = \begin{cases} 1 & |\theta| = \pi, \\ \operatorname{sgn}(\varphi_x r_y - \varphi_y r_x) & |\theta| \neq \pi. \end{cases}$$

Finally we may calculate  $\theta$  as

$$\theta = |\theta| \cdot \operatorname{sgn}(\theta).$$

Now that we have established all of the analysis procedures performed on both the mCh and GFP images, we finally can examine the results from the data.

## 5 Results

Using the cellpose cell segmentation and TrackMate data collected as described in §4, along with the data from the oxygen sensor analyzes as in §3, we can examine relations between cell speed and various properties of interest such as cell area, oxygen gradients and oxygen consumption rates. For all data in this section, a cell's displacement between times  $t$  and  $t + 1$  was compared with the median of the quantity of interest (oxygen concentration, gradients, etc.) over the area occupied by the cell at time  $t$ . We begin with the SH trial results and then proceed to the LH trial.

### 5.1 SH Trial Results

The PC3 cell speed roughly demonstrated the logical expectations that speed should decrease at lower  $[O_2]$  concentrations, lower  $[O_2]$  gradient magnitudes and lower  $O_2$  consumption rates as shown in Figure 15. From Figure 15(a) we note that hypoxia developed rather suddenly within the cell tracking region between  $t = 2$  and  $t = 3$ . Furthermore the overall speeds of the population of cells generally decreased from  $t = 3$  to 5. In (b) we see that cell speeds remain high at all gradient magnitudes at  $t = 2$ . At  $t = 3$  we see a slight trend of cells in regions of steeper gradients showing higher speed. At  $t = 4$  and 5 gradients were low throughout the region and speeds continued to decrease.

In Figure 15(c) recall that we used the sign convention that negative values indicate  $O_2$  consumption. As expected the vast majority of cells are consuming oxygen. The cells that seem to be producing oxygen may be in regions with calculation errors possibly either due to inaccuracies in the mCh correction or the  $\nabla^2$  and  $\frac{d}{dt}$  approximations in §3.3. We note that the overall  $O_2$  consumption stays relatively consistent from  $t = 2$  to  $t = 3$  but then decreases in magnitude from  $t = 3$  to  $t = 4$  and remains low at  $t = 5$ . Lastly we can clearly see in Figure 15(d) the overall decrease in cell speeds over time but a relation between cell area and speed remains unclear. To further investigate we next examine a plot similar to Figure 15(a) but with the data filtered to include only the smallest and largest cells in Figure 16.

---

<sup>4</sup>Recall that the sign function is defined as  $\operatorname{sgn} x := \begin{cases} -1 & x < 0, \\ 0 & x = 0, \\ 1 & x > 0. \end{cases}$

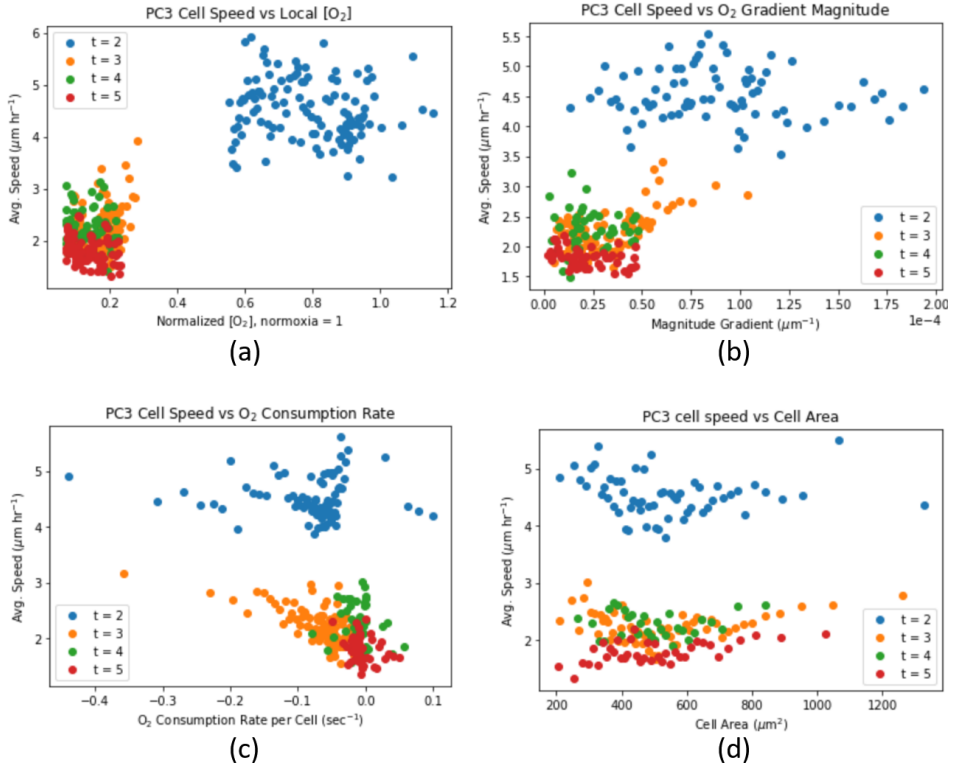


Figure 15: Binned scatter plots showing the speed of the PC3 cells in the SH trial (as determined from their frame to frame displacements) in comparison to (a) local  $O_2$  concentration, local  $O_2$  gradient magnitude, (d)  $O_2$  consumption and (d) cell area.

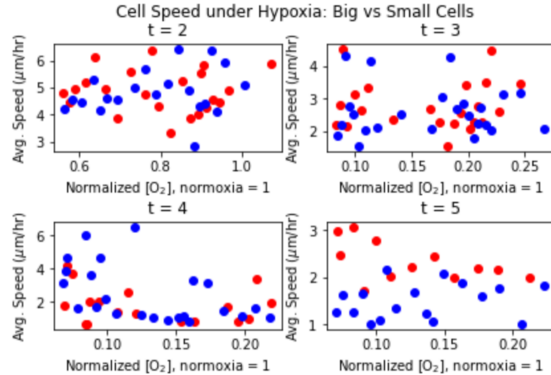


Figure 16: Binned scatter plots showing the motility of big vs small PC3 under various stages of hypoxia. Blue dots indicate cells with area under  $300 \mu\text{m}^2$  while red dots indicate cells with area over  $1000 \mu\text{m}^2$ . Note that the scaling of the x and y axes do not coincide for the four plots.

In Figure 16, we see that small and large PC3 cells do not show noticeably significant differences in motility at  $t = 2, 3, 4$ . However, after longer exposure to hypoxia at  $t = 5$ , the larger cells seem to show slightly higher motility over all  $O_2$  concentrations present in the tracking region.

A similar result was found for the LH trial as discussed in §5.2.

Lastly we examine whether the PC3 cells exhibited aerotaxis, that is, cell movement towards optimal oxygen concentrations. Previous studies have found that eukaryotic cells such as *Dictyostelium* cells [19] [20] [21] and breast tumor cells [22] exhibit aerotaxis under hypoxic conditions. Unfortunately we were unable to find indications of aerotactic behavior among our PC3 cells as shown in Figure 17.

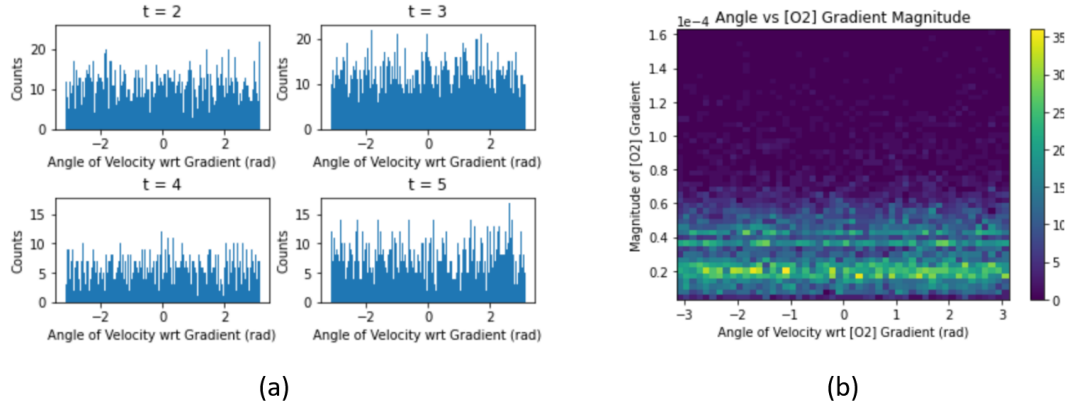


Figure 17: (a) Histograms of the angles between PC3 cell velocity and local  $[O_2]$  gradients at various times  $t$  during the SH trial. (b) A 2D histogram of gradient magnitude and angle for the  $t = 3$  data.

Notice in Figure 17(a) that at all times  $t = 2$  to  $5$  that the cell motion appears to move in random directions rather than along ( $\theta = 0$ ) or against ( $\theta = \pm\pi$ ) the  $O_2$  gradient. We also sorted cells by gradient magnitude with the idea that cells in regions of high gradients would be more likely to exhibit aerotaxis. We performed this analysis only for the data at time  $t = 3$  in Figure 17(b) since oxygen concentrations are still near normoxia at  $t = 2$  and the gradient magnitudes are uniformly low at  $t = 4$  and  $5$ . However even cells in higher  $O_2$  gradient regions still failed to show any preference for particular directions of motion with respect to the  $O_2$  gradient.

Although surprising there are some possible explanations for the result. Given that the PC3 cells form a dense confluent layer on the Lumox plate, the direction of cell motion may be influenced more local variations in cell density rather than  $O_2$  gradients. It's also possible that the  $O_2$  gradients were too low in magnitude or changed too quickly over time to allow the cells demonstrate measureable aerotaxis. In a broader view, we also did not observe any rings of outward moving cells as was observed in the *Dictyostelium* aerotaxis experiments [20].

## 5.2 LH Trial Results

The LH trial generally showed similar results as the SH trial but also demonstrated strong trends between cell motility,  $O_2$  concentrations and gradient magnitudes especially in high stress regions as shown in Figure 18.

We note in Figure 18(a) that motility and local  $[O_2]$  remains high for times  $t = 2$  to  $4$ . Then for times after  $t = 5$ ,  $[O_2]$  and motility both drop steeply for some cells while remaining high for others. From Figure 18(b) we note the peculiar trend of increasing motility even as local  $[O_2]$  begins to drop. One possible explanation is that the PC3 have not yet completely settled

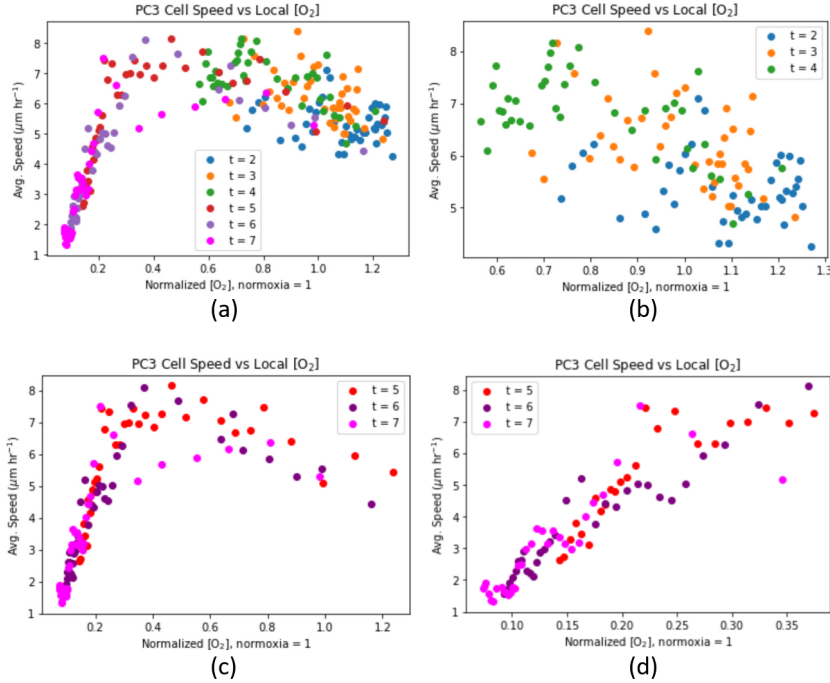


Figure 18: (a) Binned scatter plot of PC3 cell speed as a function of local  $[\text{O}_2]$  for times  $t = 2$  to 7. For clarity the cell speed data for times  $t = 2$  to 4 and times  $t = 5$  to 7 are separated into distinct plots in (b) and (c). A closer examination of (c) for  $[\text{O}_2] < 0.4$  is given in (d).

and attached to the Lumox plate at hypoxia onset and thus have not reached full motility yet. Meanwhile, the local  $[\text{O}_2]$  had not yet fallen enough to inhibit motion.

In Figure 18(c) we see that cell motility remains high and varied in regions where  $[\text{O}_2] > 0.4$  but drops roughly linearly with  $[\text{O}_2]$  for  $[\text{O}_2] < 0.4$  (see Figure 18(d)), suggesting that oxygen concentrations lower than 40% normoxia are required to inhibit cell motion (notice this is consistent with the SH trial data from Figure 15). The linear relation between speed and  $[\text{O}_2]$  appears to remain roughly constant over times  $t = 5$  to 7 but with cells increasingly tending towards lower oxygen concentrations as hypoxia continues to develop.

The presence of such a clear relation between speed and  $[\text{O}_2]$  in Figure 18(d) is somewhat puzzling given that such a trend was imperceptible in the SH trial. One immediate explanation is that the LH tracking region contained more cells within regions of intermediate values of  $[\text{O}_2]$  such as  $[0.2, 0.4]$  while the SH trial did not. In the SH trial, a large majority of the imaged cells were immersed in highly hypoxic conditions with only the extreme edges showing milder hypoxia. Additionally, the LH hypoxia developed more slowly perhaps allowing enough time for the cells to physiologically adjust to their surrounding oxygen concentrations. Also perhaps the more precise segmentation in the LH trial allowed for greater precision in measuring small cell displacements.

We next examine motility as a function of cell area in Figure 19. First notice that cell motility increases for  $t = 2$  to 5 and then decreases for  $t = 5$  to 7 across all cell sizes. Also, cells of intermediate size exhibited the largest changes in motility while the largest cells showed less change, in contrast with the SH results where the motility changes were fairly uniform across

cell sizes. We also performed the same comparison of motility of small and large PC3 cells as in the SH trial in Figure 20. Consistent with the SH trial, we note that small and big cells have comparable motility at early stages of hypoxia but for  $t > 4$ , larger cells demonstrated greater motility across all oxygen concentrations.

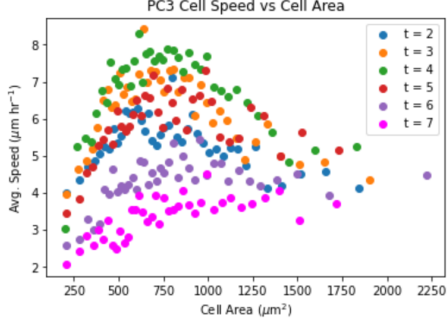


Figure 19: Binned scatter plot showing PC3 cell speed as a function of cell area after exposure to hypoxia for 2 to 7 hours.

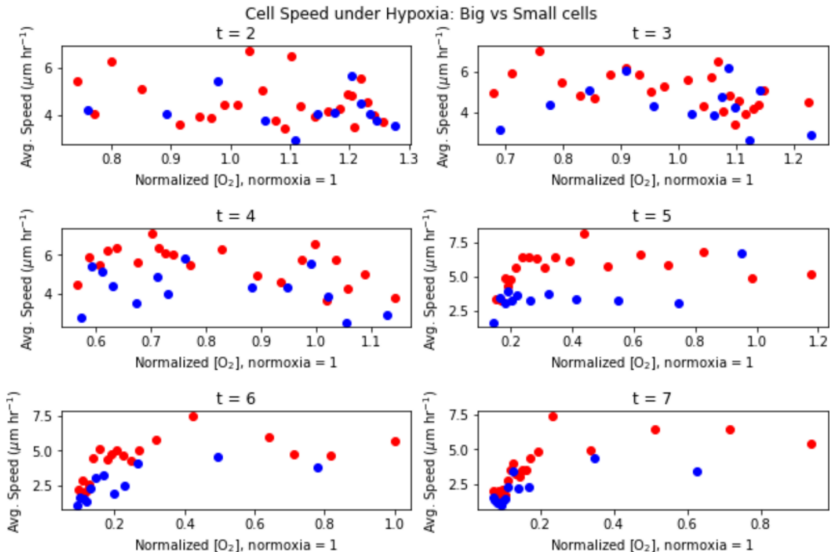


Figure 20: Binned scatter plots showing motility of big and small PC3 cells under various stages of hypoxia. Blue dots indicate cells with area under  $300 \mu \text{m}^2$  and red dots indicate cells with area over  $1200 \mu \text{m}^2$ .

We next examine the LH data for evidence of aerotaxis. We found a noticeable correlation between motility and  $[O_2]$  gradient magnitude as shown in Figure 21. The trends between cell motility and  $[O_2]$  gradient magnitudes are similar to the trends with  $O_2$  concentration, with motility remaining high across all magnitudes for  $t = 2$  to 4 and showing a strong correlation with magnitudes for  $t = 5$  to 7 particularly in at low magnitudes (the high stress region). In fact, we will show in §5.2.1 that oxygen concentration and gradient magnitude were tightly coordinated in the LH trial at times  $t = 5$  to 7.

Unfortunately, we again found a lack of directionality in movement as shown in Figure 22, suggesting that the cell movement is not a direct response to local oxygen gradients and thus likely is not aerotaxis. We note in Figure 22(a) that there are no obvious directional correlation between the cells' velocity and  $[O_2]$  gradients at all times  $t$ . Even cells in higher gradient magnitude regions in  $t = 5$  and 6 failed to demonstrate directional movement with respect to the local oxygen gradients as shown in Figure 22(b).

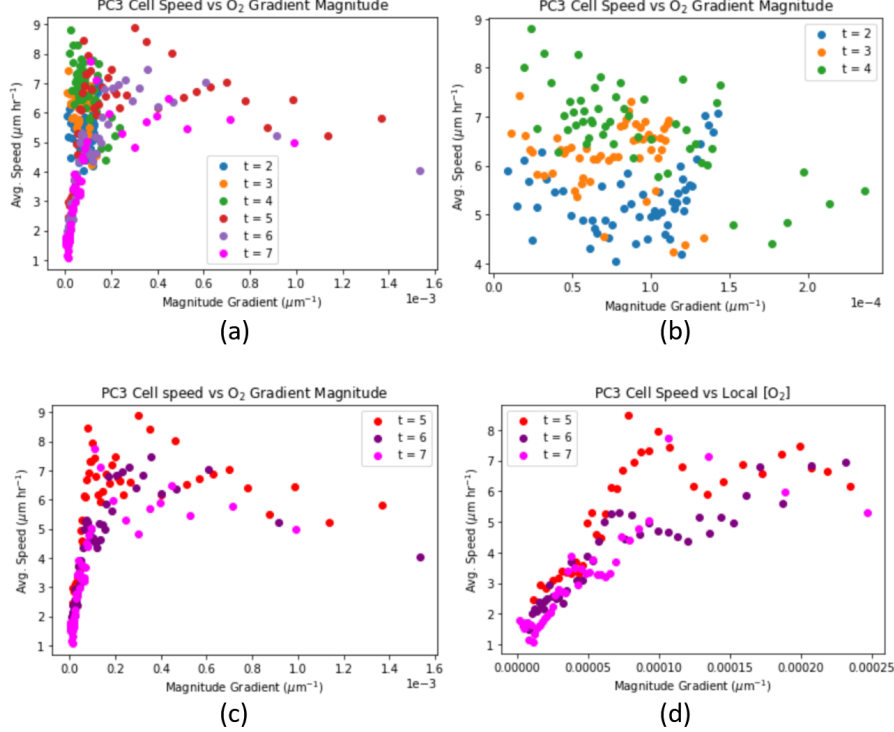


Figure 21: (a) Binned scatter plot showing PC3 cell speed as a function of the local oxygen gradient magnitude for times  $t = 2$  to 7 (b),  $t = 2$  to  $t$  and (c)  $t = 5$  to 7. Plot (d) is identical to plot (c) but displaying data points limited to low magnitude gradient regions i.e. gradient magnitude  $< 2.5 \cdot 10^{-4} \mu\text{m}^{-1}$

Lastly, we examine cell motility as a function of oxygen consumption rate in Figure 23. We note in Figure 23(b) that consumption seems to increase slightly from  $t = 2$  to 4, which is plausible since severe hypoxia has not developed yet. Starting at  $t = 5$  and onwards there is a clear tendency for cells with lower motility to also consume less  $O_2$ . Overall oxygen consumption across the population of cells seems to decrease which is plausible since the cells are impacted by severe hypoxia during this time period. Before concluding we examine one final relation to aid the justification for the lack of aerotaxis despite the strong motility vs gradient magnitude correlation.

### 5.2.1 Oxygen concentration vs. gradient magnitude

Figure 24 demonstrates the clear relation between oxygen concentration and gradient magnitude in the LH trial at  $t = 5$  to 7 in low  $[O_2]$  regions. We give a loose argument for why such a

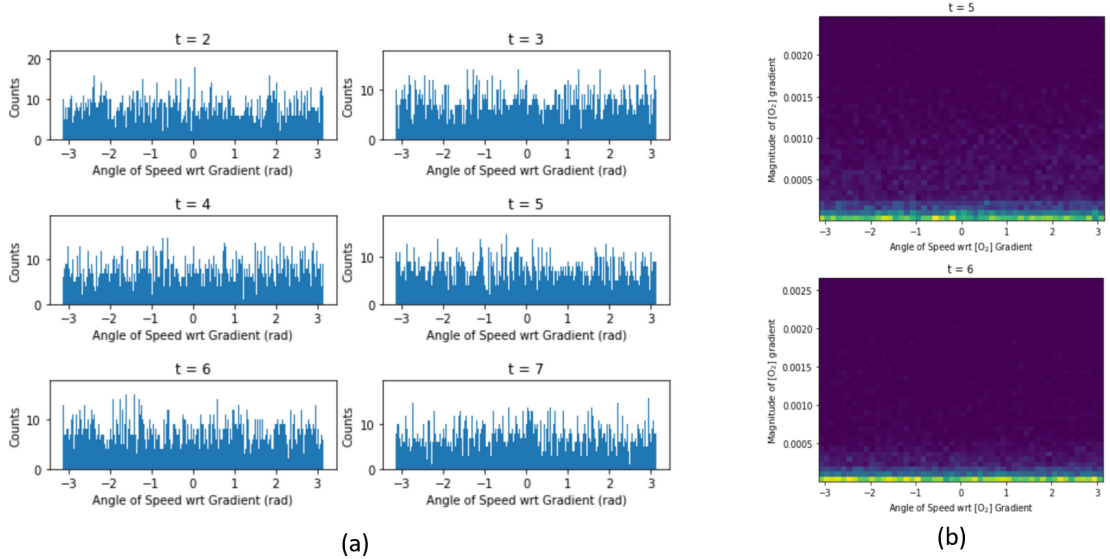


Figure 22: (a) Histograms of angles of cell velocity with respect to local  $[O_2]$  gradient vectors. (b) 2D histogram of  $[O_2]$  gradient magnitude and velocity-gradient angles for the  $t = 5$  and  $t = 6$  data.

clear relation is plausible. Suppose we have 2D region of cells of constant spatial density and constant oxygen consumption rate. Then by Fick's second law at a steady state ( $\frac{d\varphi}{dt} = 0$ ) the local oxygen concentration  $\varphi$  must satisfy  $\nabla^2 \varphi = C$  for some constant  $C > 0$ . We can assume that  $\varphi$  is radially symmetric so  $\varphi = \varphi(r)$  and it follows that  $\frac{d^2\varphi}{dr^2} = C$ .

Then  $\varphi(r) = C_1 r^2 + C_2 r + C_3$  for some constants  $C_1, C_2, C_3$  where  $C_1 > 0$ . Assuming that  $\frac{d\varphi}{dr}|_{r=0} = 0$  then we must have  $C_2 = 0$ . From the condition that  $\varphi(r) > 0$  for all  $r$  then  $C_3 > 0$ . It follows that  $|\nabla\varphi| = |\frac{d\varphi}{dr}| = 2C_1 r$ . Thus  $\varphi(|\nabla\varphi|) = \frac{|\nabla\varphi|^2}{4C_1} + C_3$  and so  $|\nabla\varphi| = \sqrt{4C_1(\varphi - C_3)}$ . Note that Figure 24 doesn't clearly demonstrate square root growth but both our assumption of constant oxygen consumption rate and steady state are not satisfied.

Based on Figure 24 we might instead estimate a roughly power law growth of  $|\nabla\varphi|$  as a function of  $\varphi$  with exponent  $1 + \epsilon$  for some small  $\epsilon > 0$ . If we assume roughly linear growth of cell motility with  $[O_2]$  then cell motility should grow with  $|\nabla\varphi|$  with a power law growth with exponent  $\frac{1}{1+\epsilon} < 1$  which roughly agrees with Figure 21(d). Thus, it is plausible that the cell speed vs magnitude gradient relation is correlational rather than causal due to the relation of both quantities to oxygen concentration.

## 6 Conclusion

In this study we investigated the dynamics of PC3 cancer cells under self-generated hypoxia using a novel phosphorescence-based oxygen sensor. Although numerous estimates and approximations were required to resolve various data issues, we still obtained some preliminary findings and demonstrated some possible uses and analyses that can be performed with phosphorescence-based oxygen sensors in combination with cell segmentation and tracking software.

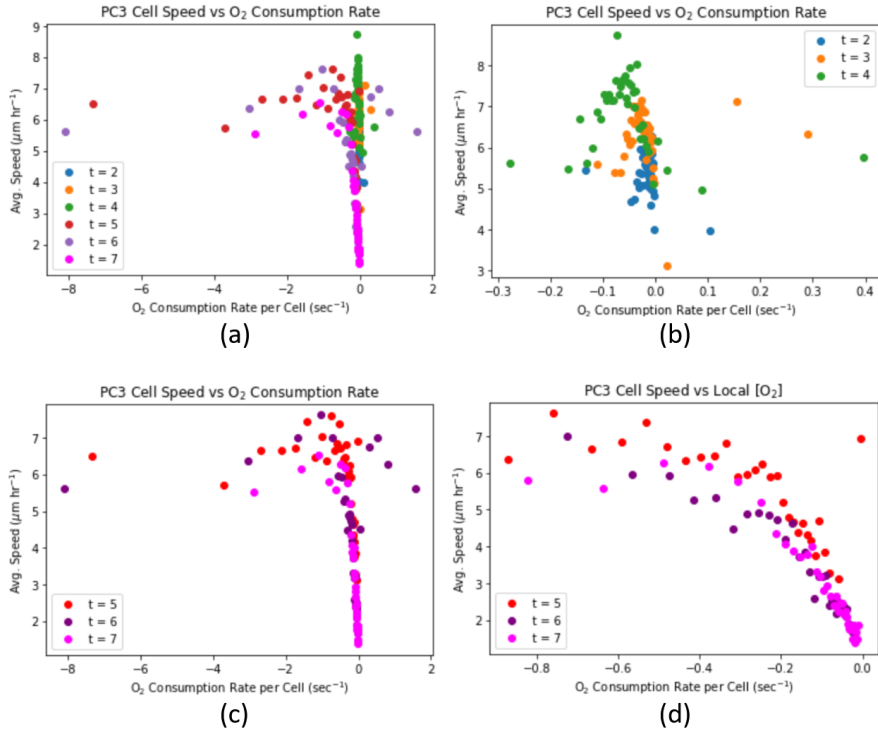


Figure 23: (a) Binned scatter plot comparing PC3 cell speed with oxygen consumption rate for  $t = 2$  to 7, (b)  $t = 2$  to 4 and (c)  $t = 5$  to 7. (d) Shows the same data points from (c) such that oxygen consumption is within the range  $(-1, 0)$

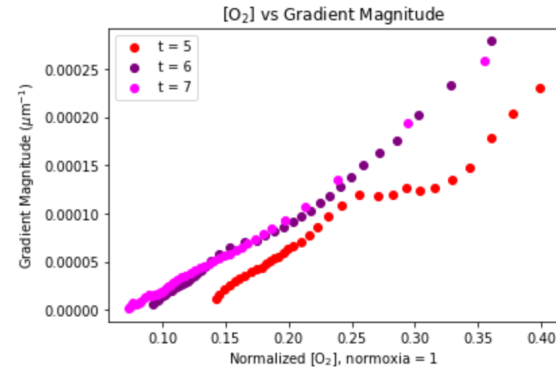


Figure 24: Binned scatter plot showing the relation between oxygen concentration and gradient magnitude in the LH trial for times  $t = 5$  to 7 in

Future experiments using phosphorescence-based oxygen sensors would benefit from illumination that is as even as possible, both so that oxygen concentrations can be accurately measured and so that the regions of cell tracking do not have to be limited to a proper subset of the image. Furthermore, cell images that are as clear and well-focused as possible will improve accuracy of cell segmentation and tracking.

In our experiments, we found positive correlations between PC3 cell speed with local oxygen concentrations, gradient magnitudes, and consumption rates. However, we were unable to find evidence that PC3 cells perform aerotaxis to escape the highly hypoxic environment. Lastly, we found a tendency for large PC3 cells to demonstrate slightly higher motility than small PC3 cells after exposure to 4 to 5 hours of self-generated hypoxia. Given the increased interest in the role of large cells (such as PACCs) and cell motility (which increases during EMT) as mediators of cancer metastasis, future investigations into the mobility of large cancer cells under hypoxic conditions as well as the aerotaxis of cancer cells would certainly contribute to the eventual goal of elucidating the mechanism of cancer metastasis and ultimately determining how to prevent it.

## Acknowledgements

I would like to thank Professor Robert H. Austin for introducing me to this intricate yet highly meaningful project and for providing numerous helpful suggestions on how to approach and analyze the data. I would also like to thank George Butler for his suggestion to validate the cell segmentation and for providing me many useful resources to do so. Additionally, I am grateful to Ken Pienta and Sarah Amend for their constructive criticism of my data analysis and for offering me advice on working with biological data. Lastly, I would like to thank Professor Peter D. Meyers for kindly agreeing to be my second reader and Nicole Ozdowski for the L<sup>A</sup>T<sub>E</sub>Xtemplate used to format this document.

## References

- [1] C. L. Chaffer and R. A. Weinberg, *A perspective on cancer cell metastasis*, science **331**, 1559 (2011).
- [2] V. Mittal, *Epithelial mesenchymal transition in tumor metastasis*, Annu Rev Pathol **13**, 395 (2018).
- [3] K. Pienta, E. Hammarlund, J. Brown, S. Amend, and R. Axelrod, *Cancer recurrence and lethality are enabled by enhanced survival and reversible cell cycle arrest of polyan euploid cells*, Proceedings of the National Academy of Sciences **118**, e2020838118 (2021).
- [4] K. J. Pienta, E. U. Hammarlund, R. Axelrod, J. S. Brown, and S. R. Amend, *Poly-aneuploid cancer cells promote evolvability, generating lethal cancer*, Evolutionary Applications **13**, 1626 (2020).
- [5] M. C. Brahimi-Horn, J. Chiche, and J. Pouysségur, *Hypoxia and cancer*, Journal of molecular medicine **85**, 1301 (2007).
- [6] J. Folkman, P. Hahnfeldt, and L. Hlatky, *Cancer: looking outside the genome*, Nature Reviews Molecular Cell Biology **1**, 76 (2000).
- [7] J. Muñoz-Sánchez and M. E. Chávez-Cárdenas, *The use of cobalt chloride as a chemical hypoxia model*, Journal of Applied Toxicology **39**, 556 (2019).
- [8] M. Kaighn, K. S. Narayan, Y. Ohnuki, J. F. Lechner, and L. Jones, *Establishment and characterization of a human prostatic carcinoma cell line (PC-3)*., Investigative urology **17**, 16 (1979).
- [9] D. G. Lowe, *Distinctive image features from scale-invariant keypoints*, International journal of computer vision **60**, 91 (2004).
- [10] Y. Zhao *et al.*, *A platinum-porphine/poly (perfluoroether) film oxygen tension sensor for noninvasive local monitoring of cellular oxygen metabolism using phosphorescence lifetime imaging*, Sensors and Actuators B: Chemical **269**, 88 (2018).
- [11] D. J. Griffiths and D. F. Schroeter, *Introduction to Quantum Mechanics* (Cambridge university press, 2018).
- [12] P. Atkins, P. W. Atkins, and J. de Paula, *Physical Chemistry* (Oxford University Press, 2014).
- [13] J. R. Lakowicz, *Principles of Fluorescence Spectroscopy* (Kluwer Academic/Plenum Publishers, 1999).
- [14] S. M. Borisov, *Fundamentals of Quenched Phosphorescence O<sub>2</sub> Sensing and Rational Design of Sensor Materials*, (2018).
- [15] P. Han and D. M. Bartels, *Temperature dependence of oxygen diffusion in H<sub>2</sub>O and D<sub>2</sub>O*, The Journal of Physical Chemistry **100**, 5597 (1996).
- [16] C. Stringer, T. Wang, M. Michaelos, and M. Pachitariu, *Cellpose: a generalist algorithm for cellular segmentation*, Nature methods **18**, 100 (2021).
- [17] D. Ershov *et al.*, *TrackMate 7: integrating state-of-the-art segmentation algorithms into tracking pipelines*, Nature Methods , 1 (2022).

- [18] J.-Y. Tinevez *et al.*, *TrackMate: An open and extensible platform for single-particle tracking*, *Methods* **115**, 80 (2017).
- [19] S. Hirose *et al.*, Aerotaxis and aerokinesis of dictyostelium discoideum under hypoxic microenvironments, in *2021 43rd Annual International Conference of the IEEE Engineering in Medicine & Biology Society (EMBC)*, pp. 1187–1190, IEEE, 2021.
- [20] S. Hirose, J.-P. Rieu, O. Cochet-Escartin, C. Anjard, and K. Funamoto, *The Oxygen Gradient in Hypoxic Conditions Enhances and Guides Dictyostelium discoideum Migration*, *Processes* **10**, 318 (2022).
- [21] M. Biondo *et al.*, *The dynamics of aerotaxis in a simple eukaryotic model*, *Frontiers in cell and developmental biology* **9**, 720623 (2021).
- [22] I. Mikaelian *et al.*, *EGFR-dependent aerotaxis is a common trait of breast tumour cells*, *Journal of Experimental & Clinical Cancer Research* **41**, 1 (2022).